

# Enhancing Ion Adsorption Capability through the Strong Interaction in Co<sub>9</sub>S<sub>8</sub>-Carbon Hybrids Achieves Superior Sodium Ion Storage

Xinyi Ma,<sup>[a]</sup> Xiaoyue He,<sup>[a]</sup> Lai Yu,<sup>[a]</sup> Nazir Ahmad,<sup>[a]</sup> Zongzhi Tao,<sup>[a]</sup> Zi Xuan Jiang,<sup>[a]</sup> Jia Cheng Liang,<sup>[a]</sup> Suyuan Zeng,<sup>[a]</sup> Liang Shi,<sup>\*[a]</sup> and Genqiang Zhang<sup>\*[a]</sup>

Metal sulfides materials are promising anode candidates for Na<sup>+</sup> storage due to their low cost and high theoretical capacity, while the complex phase transition and inevitable volume expansion during cycling restrain their practical applications. Herein, a simple one-pot manipulation strategy was designed to construct Co<sub>9</sub>S<sub>8</sub> nanoparticles strongly encapsulated in carbon nanotubes (Co<sub>9</sub>S<sub>8</sub>@C/NTs) composite structure with enhanced structural stability and reaction kinetics, resulting in greatly improved Na<sup>+</sup> storage performance. Specifically, the obtained Co<sub>9</sub>S<sub>8</sub>@C/NTs could exhibit a remarkable capacity of 500 mAh g<sup>-1</sup> at 0.5 A g<sup>-1</sup> after 100 cycles and exceptional cycling stability over 600 cycles with 88% capacity retention at 1 A g<sup>-1</sup>.

Furthermore, the theoretical calculations combined with systematic characterizations confirm that the strong interaction between Co<sub>9</sub>S<sub>8</sub> and the carbon matrix could greatly enhance the Na<sup>+</sup> adsorption ability and facilitate the electron transfer dynamics for superior Na<sup>+</sup> storage capability. More importantly, the full cell device can deliver an outstanding energy density of 144.32 Wh kg<sup>-1</sup> and a decent cycling life with 82% capacity retention of almost 100 cycles at 0.1 A g<sup>-1</sup>. This work could provide more valuable insights for designing advanced metal sulfide nanocomposites and demonstrate fascinating prospects for commercial application.

## 1. Introduction

Sodium-ion batteries have increasingly emerged as potential alternatives to their lithium-ion counterparts owing to their abundant natural reserves, low cost, and similar charge/discharge mechanism.<sup>[1]</sup> Unfortunately, the larger ionic radius of Na<sup>+</sup> (1.02 Å) than that of Li<sup>+</sup> (0.76 Å) could inevitably induce severe volume variation and sluggish ion diffusion kinetics in electrode materials during the Na<sup>+</sup> intercalation/extraction process, leading to limited specific capacity and inferior cycling stability.<sup>[2]</sup> Thus, designing appropriate electrode materials with satisfactory electrochemical performance is imperative to push forward the future development for SIBs.<sup>[2b,d,3]</sup>

Among various electrode materials, metal sulfides, especially cobalt sulfide (Co<sub>9</sub>S<sub>8</sub>), featuring high theoretical capacity, remarkable electrochemical reversibility and ideal thermal and mechanical stability hold as one of the most prospective anode candidates for sodium-ion energy storage.<sup>[4]</sup> Nevertheless, they generally confront with the complex phase transition process that could cause the dramatic volumetric variation and inferior diffusion kinetics upon charge/discharge process, resulting in

unsatisfied reversible capability and rapid capacity fading.<sup>[2d,5]</sup> To tackle these issues, the construction of metal sulfide/carbon composites has been confirmed as an effective approach to optimizing the electrochemical performance by enhancing structural stability, boosting electrical conductivity, and promoting charge transfer dynamics.<sup>[3e,4b,6]</sup> For instance, Zhang et al. constructed a Co<sub>9</sub>S<sub>8</sub>/HNCS composite with well-defined cobalt sulfide nanoparticles homogeneously encapsulated in 3D hollow nitrogen-doped carbon shells, enhancing the overall electrical conductivity and reaction kinetics, thus presenting an impressive reversible capacity and exceptional cycling stability.<sup>[2d]</sup> Besides, the Goodenough group manufactured Co<sub>9</sub>S<sub>8</sub> nanotubes wired by Co<sub>9</sub>S<sub>8</sub>-C composite nanofibers to form a fiber-in-tube structure, effectively buffering the detrimental volumetric transformation, offering a conductive pathway for electrons and greatly elevating power density.<sup>[6a]</sup> Despite these remarkable achievements, several significant concerns still need to be resolved to facilitate the development of SIBs. Firstly, designing advanced metal sulfide/carbon composites in a simpler and more efficient way is highly urgent to meet the standards of future large-scale manufacturing. Secondly, the deeper investigation in reaction mechanism during cycling is still deficient to reveal the origins of the enhanced storage capability. Moreover, more theoretical analyses need to be conducted to explore the relationship between the complex material structure and optimized electrochemical performance. Besides, achieving a favorable energy density of electrode materials in the full cell device is still a pivotal issue that needs to be addressed for future practicability.

Herein, a simple and feasible strategy was proposed to strongly encapsulate Co<sub>9</sub>S<sub>8</sub> nanoparticles in carbon nanotubes

[a] X. Ma, X. He, L. Yu, N. Ahmad, Z. Tao, Z. X. Jiang, J. C. Liang, Prof. S. Zeng, Prof. L. Shi, Prof. G. Zhang  
Hefei National Research Center for Physical Sciences at the Microscale, CAS Key Laboratory of Materials for Energy Conversion, Department of Materials Science and Engineering, University of Science and Technology of China, Hefei, Anhui 230026 China  
E-mail: gqliang@ustc.edu.cn  
gqzhangmse@ustc.edu.cn

 Supporting information for this article is available on the WWW under <https://doi.org/10.1002/batt.202400170>

( $\text{Co}_9\text{S}_8@\text{C/NTs}$ ) as an anode material for SIBs. The intense interaction between the  $\text{Co}_9\text{S}_8$  nanoparticles and carbon nanotubes in the composite structure could inhibit  $\text{Co}_9\text{S}_8$  nanoparticles from aggregation and pulverization, suppress the volume expansion, facilitate the ion diffusion kinetics and provide abundant reaction sites, thus greatly enhancing the  $\text{Na}^+$  storage ability. Accordingly, the obtained  $\text{Co}_9\text{S}_8@\text{C/NTs}$  could deliver a pronounced specific capacity of  $500 \text{ mAh g}^{-1}$  at a rate of  $0.5 \text{ A g}^{-1}$  after 100 cycles. Moreover, an outstanding cycling performance of  $423 \text{ mAh g}^{-1}$  over 600 cycles with an 88% retention rate at  $1 \text{ A g}^{-1}$  could be achieved. Particularly, the density functional theory calculations integrated with a series of ex situ measurements were employed to reveal that the synergistic effect between the  $\text{Co}_9\text{S}_8$  nanoparticles and carbon nanotubes matrix could facilitate the absorption kinetics of  $\text{Na}^+$  and promote the electron transfer behavior. Most significantly, the assembled full cell device with  $\text{Co}_9\text{S}_8@\text{C/NTs}$  anode and  $\text{Na}_3\text{V}_2(\text{PO}_4)_3/\text{C}$  cathode could accomplish a brilliant energy density of  $144.32 \text{ Wh kg}^{-1}$  along with a fabulous retention rate of 82% nearly 100 cycles at  $0.1 \text{ A g}^{-1}$ , manifesting the promising prospects for practical commercialization.

## 2. Results and Discussion

The schematic illustration of the synthesis route for  $\text{Co}_9\text{S}_8@\text{C/NTs}$  is illustrated in Figure 1a. Briefly, the  $\text{CoS}_x\text{-NTs}$  precursor consisting of interlaced nanotubes was obtained by a facile one-step solvothermal process with a mixture of melamine,  $\text{Co}(\text{NO}_3)_2 \cdot 6\text{H}_2\text{O}$  and 2-thiobarbituric acid (TBA) in ethanol medium (Figure S1, Supporting Information). After high-temperature calcination in an argon atmosphere, the initially smooth nanotubes of the  $\text{CoS}_x\text{-NTs}$  precursor transformed into uneven nanotubes of  $\text{Co}_9\text{S}_8@\text{C/NTs}$  that were robustly embedded with  $\text{Co}_9\text{S}_8$  nanoparticles. As illustrated in Figure 1b and Figure S2, Supporting Information, the characteristic peaks observed in both  $\text{Co}_9\text{S}_8@\text{C/NTs}$  and pristine  $\text{Co}_9\text{S}_8$  aligning well with the standard  $\text{Co}_9\text{S}_8$  pattern (JCPDS 86-2273)<sup>[7]</sup> confirming the successful synthesis and crystal structure of  $\text{Co}_9\text{S}_8$ . The existence of carbon in the  $\text{Co}_9\text{S}_8@\text{C/NTs}$  and pristine  $\text{Co}_9\text{S}_8$  were further confirmed by Raman spectroscopy (Figure S3, Supporting Information). Two distinct Raman peaks observed at  $1338$  and  $1590 \text{ cm}^{-1}$  relate to the typical D-band (disordered) and G-band (graphitic) of carbon, respectively.<sup>[8]</sup> The intensity ratio of  $I_{\text{D}}/I_{\text{G}}$  for  $\text{Co}_9\text{S}_8@\text{C/NTs}$  (1.1) is higher than that of pristine  $\text{Co}_9\text{S}_8$  (1.09), suggesting that  $\text{Co}_9\text{S}_8@\text{C/NTs}$  possesses more active sites and defects by integrating with carbon matrix, which could be favorable to sodium-ion storage and electron diffusion

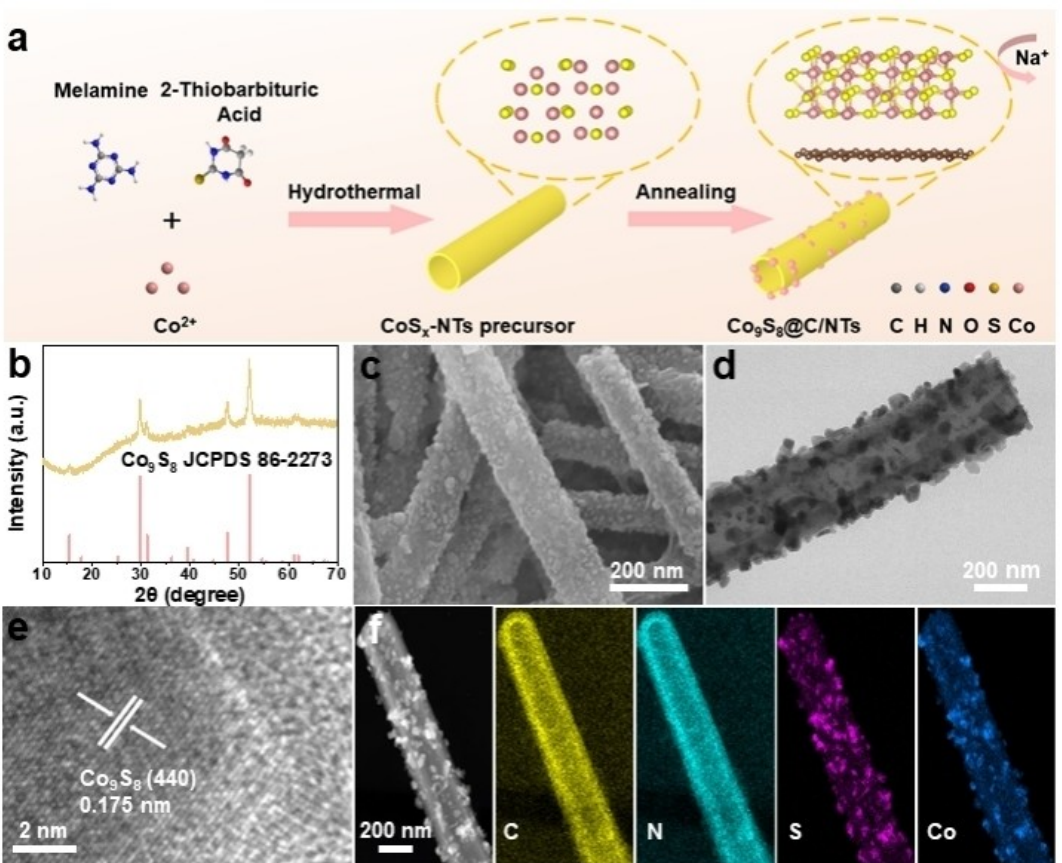


**Figure 1.** Morphological and microstructural characterization of  $\text{Co}_9\text{S}_8@\text{C/NTs}$ . (a) Schematic illustration of the synthetic process; (b) XRD pattern; (c) FESEM and (d) TEM images; (e) HRTEM analysis; (f) HAADF image and EDS mapping results.

kinetics.<sup>[9]</sup> The detailed morphology and microstructure of the Co<sub>9</sub>S<sub>8</sub>@C/NTs were further characterized by field emission scanning electron microscopy (FESEM) and transmission electron microscopy (TEM) analyses. The SEM and TEM images (Figure 1c, d) manifest that the nanosized Co<sub>9</sub>S<sub>8</sub> particles are highly embedded into the carbon nanotubes. In contrast, the product without adding melamine displays irregular morphology as shown in FESEM and TEM (Figure S4, Supporting Information). The high-magnification TEM (Figure S5, Supporting Information) shows that the Co<sub>9</sub>S<sub>8</sub> nanoparticles are wrapped with amorphous carbon, accommodating the volume expansion and improving the electrical conductivity. The absence of distinct lattice of carbon can be ascribed to its amorphous nature. In contrast, as revealed in the high-resolution TEM (HRTEM) image (Figure 1e), the clear lattice fringes with an interlayer spacing of 0.175 nm are associated

with the (440) crystal plane of Co<sub>9</sub>S<sub>8</sub>.<sup>[10]</sup> which is in line with the XRD pattern (Figure 1b). Moreover, the energy-dispersive spectroscopy (EDS) mapping results (Figure 1f) further indicate that C and N are uniformly dispersed in the whole structure, while the S and Co are mainly distributed in the core part of the Co<sub>9</sub>S<sub>8</sub> nanoparticles, verifying the embedding architecture of Co<sub>9</sub>S<sub>8</sub> nanoparticles incorporating into the carbon matrix can be successfully acquired. Additionally, the mass fraction of Co<sub>9</sub>S<sub>8</sub> in this hybrid structure is figured out to be 63.31%, as demonstrated in Figure S6, Supporting Information.

The surface electronic states and chemical composition of Co<sub>9</sub>S<sub>8</sub>@C/NTs were further explored by X-ray photoelectron spectroscopy (XPS). As disclosed in Figure 2a, the survey spectrum of Co<sub>9</sub>S<sub>8</sub>@C/NTs reveals the signals of Co, S, N, and C elements, which are consistent with the EDS mapping results. For the high-resolution Co 2p spectrum (Figure 2b), the

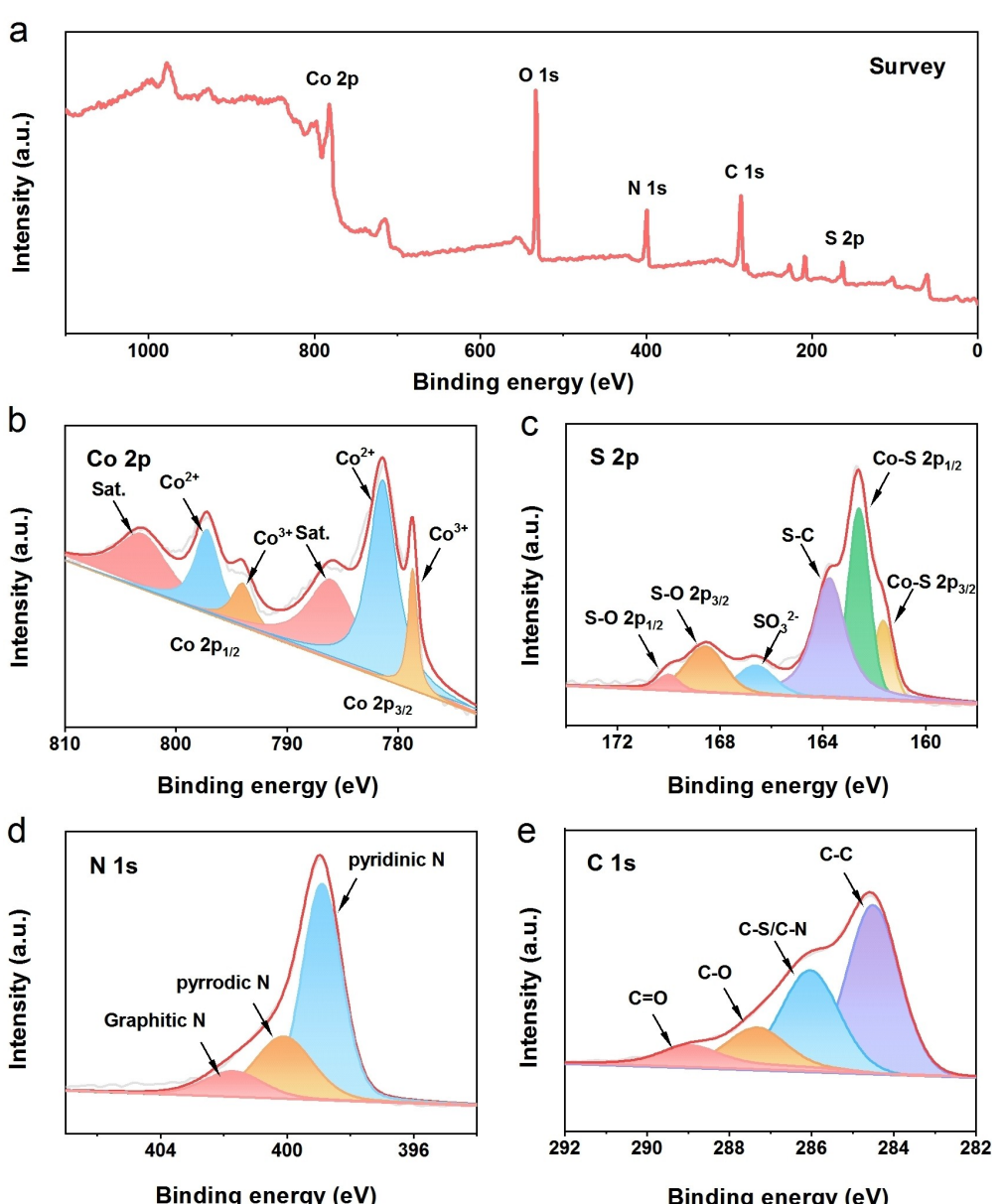
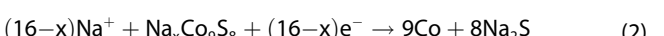
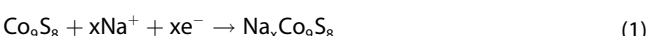


Figure 2. XPS analysis of Co<sub>9</sub>S<sub>8</sub>@C/NTs. (a) Survey spectrum, (b) Co 2p, (c) S 2p, (d) N 1s, and (e) C 1s.

dominant peaks identified at 778.8 and 794.1 eV belong to  $2p_{3/2}$  and  $2p_{1/2}$  core levels of  $\text{Co}^{3+}$ , while those peaks located at 781.4 and 797.3 eV are indexed to  $2p_{3/2}$  and  $2p_{1/2}$  core levels of  $\text{Co}^{2+}$ , respectively. Besides, the other two peaks centered at 786.2 and 803.3 eV can be ascribed to the shaking-up satellite peaks (denoted as Sat.).<sup>[9,11]</sup> Moreover, there are six peaks at 161.7, 162.6, 163.8, 166.6, 168.6, and 170.0 eV in the S 2p spectrum (Figure 2c), which can be attributed to Co–S  $2p_{3/2}$ , Co–S  $2p_{1/2}$ , C–S,  $\text{SO}_3^{2-}$ , S–O  $2p_{3/2}$  and S–O  $2p_{1/2}$ , separately. The appearance of Co–S and C–S emphasizes S atoms were successfully incorporated into the carbon matrix and combined with Co to form cobalt sulfides, and then the cobalt sulfides nanoparticles strongly interact with the carbon nanotube matrix.<sup>[12]</sup> What is more, the existence of S–O was associated with the inevitable oxidation of the S species when exposed to the air.<sup>[3e,13]</sup> As shown in Figure 2d, the N 1s spectrum can be deconvoluted to three peaks at 398.9, 400.1, and 401.8 eV, which are related to pyridinic N, pyrrolic N, and graphitic N,<sup>[14]</sup> respectively, suggesting the introduction of nitrogen into carbon matrix.<sup>[4b,15]</sup> The C 1s spectrum of  $\text{Co}_9\text{S}_8@\text{C/NTs}$  (Figure 2e) can be divided into four peaks located at 284.5, 286.1, 287.4, and 289.0 eV, which can be assigned to the C–C, C–S/C–N, C–O, and C=O bonds, respectively, further certifying the existence of the strong C–S bond and the perfect addition of sulfur into carbon nanotubes configuration.<sup>[4b,10a, 16]</sup> The above results further manifest the chemical elements of  $\text{Co}_9\text{S}_8@\text{C/NTs}$ , which is constant with the

XRD pattern and EDS mapping results mentioned above. The Brunauer-Emmett-Teller (BET) measurement (Figure S7, Supporting Information) results imply a relatively larger specific surface area of  $\text{Co}_9\text{S}_8@\text{C/NTs}$  ( $92.01 \text{ m}^2 \text{ g}^{-1}$ ) than that of pristine  $\text{Co}_9\text{S}_8$  ( $54.64 \text{ m}^2 \text{ g}^{-1}$ ), which can shorten the diffusion path and facilitate rapid ion adsorption, thus benefitting faster charge storage kinetics.<sup>[17]</sup>

Figure 3a demonstrates the cyclic voltammetry (CV) profiles of the first three cycles of  $\text{Co}_9\text{S}_8@\text{C/NTs}$  composite within a voltage range of 0.1–3.0 V at a scan rate of  $0.1 \text{ mV s}^{-1}$ . During the first cathodic scan, the tiny peak at 0.9 V corresponds to the  $\text{Na}^+$  intercalation into  $\text{Co}_9\text{S}_8@\text{C/NTs}$  and the occurrence of the conversion reaction:<sup>[4a,b,18]</sup>



Moreover, a distinct irreversible peak that appears at 0.6 V could be due to the decomposition of the electrolyte and the formation of a solid electrolyte interface (SEI) on the surface of the electrode.<sup>[18]</sup> In the corresponding anodic scan, the peak identified at 1.7 V could be ascribed to the extraction of the sodium ions from the  $\text{Co}_9\text{S}_8@\text{C/NTs}$  composite, suggesting the occurrence of the reverse conversion reaction.<sup>[4b,18]</sup> The subsequent CV cycles of  $\text{Co}_9\text{S}_8@\text{C/NTs}$  almost overlap compared to

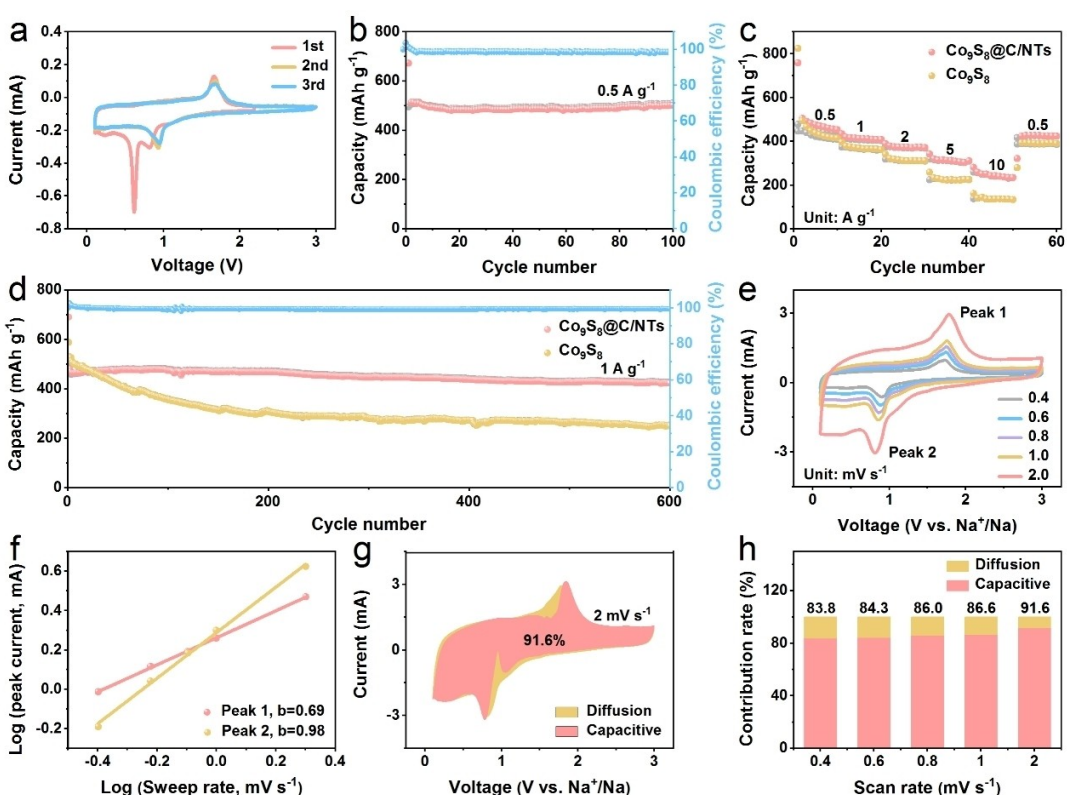


**Figure 3.** Electrochemical performance of  $\text{Co}_9\text{S}_8@\text{C/NTs}$  anode for SIBs. (a) CV curves at  $0.1 \text{ mV s}^{-1}$ ; (b) galvanostatic charge/discharge profiles at  $0.5 \text{ A g}^{-1}$ ; (c) rate capability at various current densities ranging from  $0.5$  to  $10 \text{ A g}^{-1}$ ; (d) cycling stability at  $1 \text{ A g}^{-1}$ ; (e) CV curves at various scan rates; (f) calculated b values from CV curves; (g) capacitive contribution at a scan rate of  $2 \text{ mV s}^{-1}$ ; (h) capacitive contribution of  $\text{Co}_9\text{S}_8@\text{C/NTs}$  to the total capacity at various scan rates.

that of pristine  $\text{Co}_9\text{S}_8$  electrode as disclosed in Figure S8, Supporting Information, reflecting superior reversibility of  $\text{Co}_9\text{S}_8@\text{C}/\text{NTs}$  composite.<sup>[4b]</sup> As illustrated in Figure 3b, the  $\text{Co}_9\text{S}_8@\text{C}/\text{NTs}$  delivers an ultra-high reversible capacity of 500  $\text{mAh g}^{-1}$  after 100 cycles at 0.5  $\text{A g}^{-1}$  with negligible capacity degradation, thus embodying distinguished electrochemical performance. Figure S9, Supporting Information, implies an initial discharge/charge capacity of 672/495  $\text{mAh g}^{-1}$  at 0.5  $\text{A g}^{-1}$ , which suggests a relatively low initial Coulombic efficiency (ICE) ascribed to the formation of a solid electrolyte interface (SEI) layer, electrolyte decomposition, and irreversible side reactions. The obvious voltage plateaus in the charge/discharge profiles are in good accordance with the CV curves. Further, the overlapped discharge/charge curves in the subsequent cycles illuminate a highly reversible electrochemical process of the  $\text{Co}_9\text{S}_8@\text{C}/\text{NTs}$  anode, corresponding to the CV curves. Markedly, the  $\text{Co}_9\text{S}_8@\text{C}/\text{NTs}$  anode also possesses excellent rate performance (Figure 3c), exhibiting considerable capacities of 505, 418, 378, 319, and 258  $\text{mAh g}^{-1}$  at rates of 0.5, 1, 2, 5, and 10  $\text{A g}^{-1}$ , respectively, which outperforms the pristine  $\text{Co}_9\text{S}_8$  electrode. Impressively, the specific capacity can be almost recovered when the current density is set back to 0.5  $\text{A g}^{-1}$ , implying the available reversibility of  $\text{Co}_9\text{S}_8@\text{C}/\text{NTs}$  for  $\text{Na}^+$  storage. More excitingly, as reflected in Figure 3d, the  $\text{Co}_9\text{S}_8@\text{C}/\text{NTs}$  extends a superb cycling performance with a capacity of 423  $\text{mAh g}^{-1}$  over 600 cycles at 1  $\text{A g}^{-1}$  with a capacity retention of 88%, which is far more stable than pristine  $\text{Co}_9\text{S}_8$  and is comparable to the previously reported work in the literature (Table S1, Supporting Information). Notably, even under higher current density at 5  $\text{A g}^{-1}$ , the  $\text{Co}_9\text{S}_8@\text{C}/\text{NTs}$  electrode could still manifest superb electrochemical performance for  $\text{Na}^+$  storage (Figure S10, Supporting Information).

Cyclic voltammetry (CV) measurement was performed at different scan rates ranging from 0.4 to 2  $\text{mVs}^{-1}$  within the voltage range of 0.1–3.0 V to gain a comprehensive understanding of the kinetic behavior and storage mechanism of the  $\text{Co}_9\text{S}_8@\text{C}/\text{NTs}$  electrode in SIBs, as shown in Figure 3e. The redox peaks show similar shapes upon the increasing scan rates, suggesting a slight polarization voltage and fast  $\text{Na}^+$  storage kinetics. The pristine  $\text{Co}_9\text{S}_8$  electrode performs unfavorable responses (Figure S11, Supporting Information). In detail, it was indicated that the relationship between the peak current and the scan rate can be described in the following equations:

$$i_{(\text{peak})} = av^b \quad (3)$$

$$\log i_{(\text{peak})} = b \log(v) + \log(a) \quad (4)$$

where  $i$  and  $v$  are index to peak current and scan rate, and  $a$  and  $b$  represent adjustable constants. Typically, the  $b$  values of 0.5 and 1.0 denote the diffusion and capacitive-controlled processes separately.<sup>[19]</sup> As unveiled in Figure 3f, the  $b$  values computed from the slope of the linear relationship between  $\log(i)$  and  $\log(v)$  are calculated to be 0.69/0.98 for the anodic/cathodic process, illustrating a capacitive-dominated storage behavior, thereby contributing to advanced rate capability. In particular, the current value can be divided into capacitive

contribution ( $k_1v$ ) and diffusion contribution ( $k_2v^{1/2}$ ) based on the following equation:<sup>[8a,20]</sup>

$$i = k_1v + k_2v^{1/2} \quad (5)$$

As calculated in Figure 3g, an exorbitant capacitive contribution of 91.6% can be attained at a scan rate of 2  $\text{mVs}^{-1}$ . Notably, the capacitive contribution gradually increases from 83.8 to 91.6% when the scan rate rises from 0.4 to 2  $\text{mVs}^{-1}$  (Figure 3h), implying a superior pseudocapacitance contribution than that of pristine  $\text{Co}_9\text{S}_8$  (Figure S11, Supporting Information). Such a high pseudocapacitive contribution was originated from the unique composite structure of highly dispersed  $\text{Co}_9\text{S}_8$  nanoparticles strongly embedded in conductive carbon nanotubes, which provides large surface area and offers abundant active sites to enhance the adsorption ability of the  $\text{Na}^+$ , thus greatly contributing to rapid charge transfer kinetics for  $\text{Na}^+$  storage.<sup>[21]</sup>

The phase transformation in  $\text{Na}^+$  insertion/extraction process of  $\text{Co}_9\text{S}_8@\text{C}/\text{NTs}$  at fully discharged/charged states during the initial cycling were investigated through ex situ XRD measurement. As depicted in Figure 4a, the diffraction peaks of  $\text{Co}_9\text{S}_8$  phases can be observed in the initial state of the open-circuit voltage. Upon full discharge to 0.1 V, the peaks of the  $\text{Co}_9\text{S}_8$  phase almost diminished while two new peaks referring to the phase of  $\text{Na}_2\text{S}$  forming at 39 and 56°,<sup>[8a,22]</sup> accompanied by the peak of Co located at 44° came into sight,<sup>[16b]</sup> which agrees well with conversion reactions from  $\text{Co}_9\text{S}_8$  phase to  $\text{Na}_2\text{S}$  and Co phases during the discharge process. After being fully charged to 3 V, the peaks of the  $\text{Co}_9\text{S}_8$  phase became visible again, accompanied by  $\text{Na}_2\text{S}$  and Co phases almost disappeared, indicating the reversible phase transformation from  $\text{Na}_2\text{S}$  and Co to  $\text{Co}_9\text{S}_8$ , thus demonstrating the ideal reversibility of  $\text{Co}_9\text{S}_8@\text{C}/\text{NTs}$  composite during the cycling process. This can also be verified by the SEM images after cycling (Figure S12, Supporting Information), further demonstrating the structural stability of the  $\text{Co}_9\text{S}_8@\text{C}/\text{NTs}$ .

To determine the  $\text{Na}^+$  ion diffusion resistance and electronic conductivity properties,<sup>[9a,19a]</sup> electrochemical impedance spectroscopy (EIS) measurement was employed to explore the charge transfer kinetics. The Nyquist plots before cycling and after 5th, 20th, 100th cycles at 0.5  $\text{A g}^{-1}$  for the  $\text{Co}_9\text{S}_8@\text{C}/\text{NTs}$  electrode are supplied in Figure 4b. Wherein the semicircles in the high-frequency region represent charge transfer resistance ( $R_{ct}$ ),<sup>[23]</sup> and the slopes in the low-frequency region correspond to Warburg impedance ( $Z_w$ ) relating to the diffusion of sodium ion.<sup>[8a]</sup> The charge-transfer resistance ( $R_{ct}$ ) of the  $\text{Co}_9\text{S}_8@\text{C}/\text{NTs}$  is much lower than that of the pristine  $\text{Co}_9\text{S}_8$  (Figure S13, Supporting Information) and gradually decreases with the increasing number of cycles, suggesting the enhanced charge transfer kinetics in the  $\text{Co}_9\text{S}_8@\text{C}/\text{NTs}$  composite. The galvanostatic intermittent titration technique (GITT) is also conducted to evaluate the rapid sodium-ion diffusion kinetic process (Figure 4c, d). According to the pioneering studies, the calculation method is validated by the following formula:<sup>[15b,24]</sup>

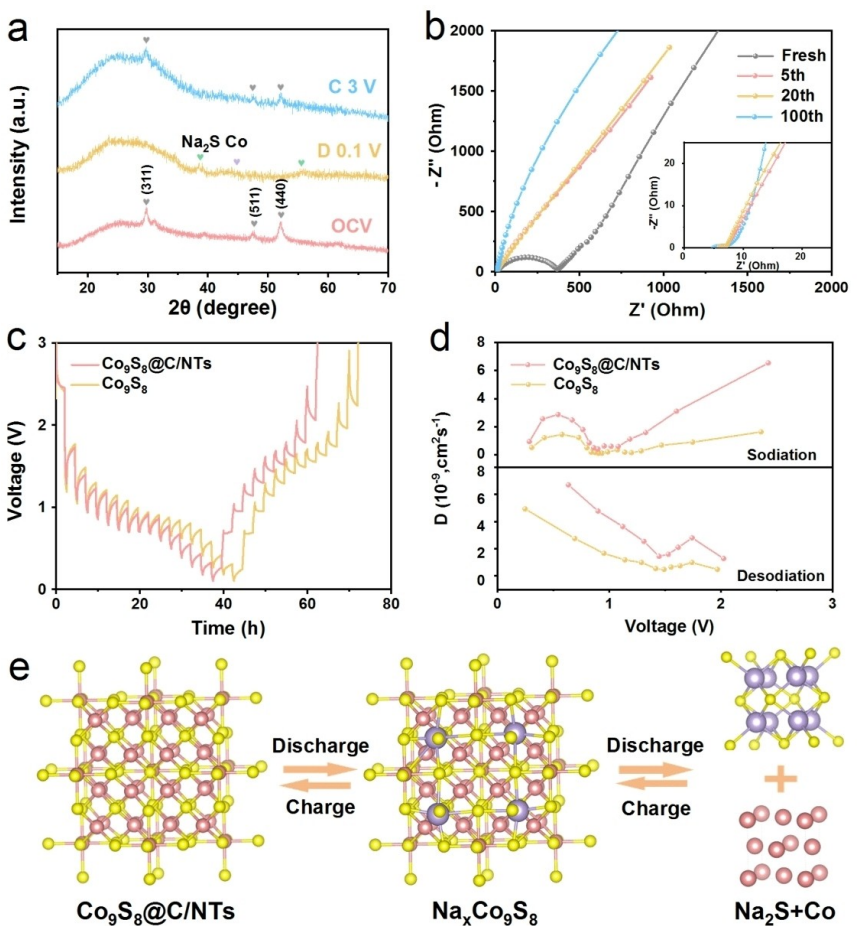


**Figure 4.** Sodium ion storage mechanism of Co<sub>9</sub>S<sub>8</sub>@C/NTs. (a) Ex-situ XRD patterns at 0.1 A g<sup>-1</sup> during the first cycle; (b) Nyquist plots at different cycles of Co<sub>9</sub>S<sub>8</sub>@C/NTs; (c) GITT profiles and (d) calculated diffusion coefficients of the first charge/discharge process at 0.1 A g<sup>-1</sup> of Co<sub>9</sub>S<sub>8</sub>@C/NTs and pristine Co<sub>9</sub>S<sub>8</sub>; (e) Schematic illustration of the structure evolution during the reversible electrochemical conversion process.

$$D = \frac{4}{\pi \tau} \left( \frac{m_B V_M}{M_B S} \right)^2 \left( \frac{\Delta E_s}{\Delta E_\tau} \right)^2 \tau \ll \frac{L^2}{D} \quad (6)$$

where  $D_{Na^+}$  (cm<sup>2</sup>s<sup>-1</sup>) is the chemical diffusion coefficient;  $V_M$  (cm<sup>3</sup>s<sup>-1</sup>),  $m_B$ , and  $M_B$  are the molar volume, mass loading, and molar weight of the active material, respectively;  $S$  and  $\tau$  denote the area of the electrode-electrolyte interface and the time duration of the current pulse;  $\Delta E_s$  and  $\Delta E_\tau$  mark the steady-state voltage change and voltage change during the current pulse, respectively. The details of the  $\Delta E_s$  and  $\Delta E_\tau$  parameters are supplemented in Figure S14, Supporting Information. Especially, as reflected in Figure 4d, the diffusion coefficient of Na<sup>+</sup> in Co<sub>9</sub>S<sub>8</sub>@C/NTs was higher than pristine Co<sub>9</sub>S<sub>8</sub> during the Na<sup>+</sup> insertion/extraction procedures, interpreting accelerated diffusion kinetics and enhanced electron conductivity in the Co<sub>9</sub>S<sub>8</sub>@C/NTs anode, thus enabling fabulous rate capability and cycling stability. Overall, the electrochemical reaction process of Co<sub>9</sub>S<sub>8</sub>@C/NTs is schematically illustrated in Figure 4e.

To understand the outstanding electrochemical properties of Co<sub>9</sub>S<sub>8</sub>@C/NTs anode material, the density functional theory (DFT) calculations were conducted to elucidate the advantages of this metal compound/carbon composite material. The geo-

metric configurations of Co<sub>9</sub>S<sub>8</sub>@C/NTs and pristine Co<sub>9</sub>S<sub>8</sub> models were optimized (Figure S15, Supporting Information), and the corresponding adsorption models of Na<sup>+</sup> and adsorption energy ( $E_{ads}$ ) were calculated as shown in Figure 5a, b. Based on the corresponding specific structures, the lower adsorption energy ( $E_{ads}$ ) of Co<sub>9</sub>S<sub>8</sub>@C/NTs (-2.22 eV) than that of pristine Co<sub>9</sub>S<sub>8</sub> (-1.01 eV) indicates that the intense combination between Co<sub>9</sub>S<sub>8</sub> nanoparticles and carbon nanotubes are beneficial to the adsorption of Na<sup>+</sup>. Moreover, the Na<sup>+</sup> migration paths and the corresponding diffusion energies of these two materials were supplied in Figure 5c, d, where a lower energy barrier of Co<sub>9</sub>S<sub>8</sub>@C/NTs manifests better electron transfer dynamics. In addition, the comparison of the density of states (DOS) calculation results (Figure 5e, f) verifies that the Co<sub>9</sub>S<sub>8</sub>@C/NTs exhibit an improved electronic state around the Fermi level compared with the pristine Co<sub>9</sub>S<sub>8</sub>, articulating higher electronic conductivity to boost the charge transfer kinetics. These theoretical investigations prove that the strong interaction between Co<sub>9</sub>S<sub>8</sub> nanoparticles and carbon nanotubes could accelerate the Na<sup>+</sup> absorption kinetics and facilitate the electron transfer behavior, which could be responsible for the superior sodium ion storage capability.

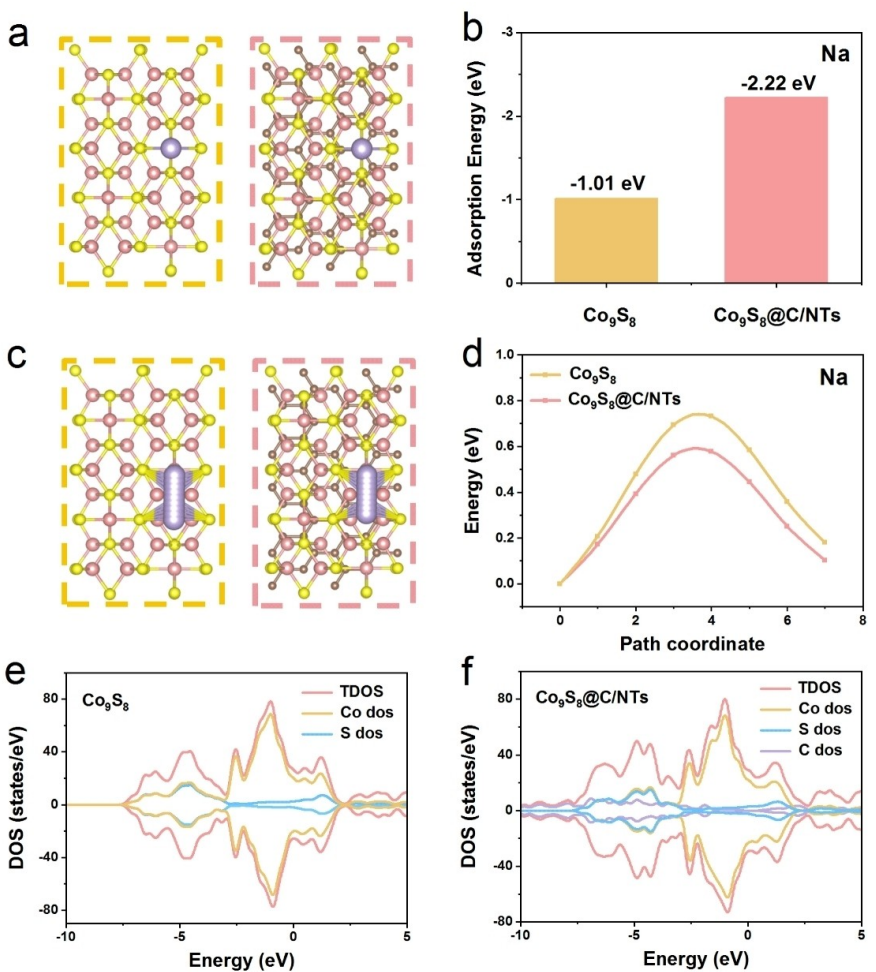


**Figure 5.** The theoretical calculation results of  $\text{Co}_9\text{S}_8@\text{C}/\text{NTs}$  for sodium ion storage. (a) The adsorption models of  $\text{Na}^+$  and (b) corresponding adsorption energy ( $E_{\text{ads}}$ ) in pristine  $\text{Co}_9\text{S}_8$  and  $\text{Co}_9\text{S}_8@\text{C}/\text{NTs}$ , respectively; (c) The migration paths in the pristine  $\text{Co}_9\text{S}_8$  and  $\text{Co}_9\text{S}_8@\text{C}/\text{NTs}$  along with (d) corresponding migration energies; The total density of states (TDOS) of (e) pristine  $\text{Co}_9\text{S}_8$  and (f)  $\text{Co}_9\text{S}_8@\text{C}/\text{NTs}$ .

To better prove the practicability for future application, the full cell device featuring  $\text{Co}_9\text{S}_8@\text{C}/\text{NTs}$  anode and commercial  $\text{Na}_3\text{V}_2(\text{PO}_4)_3/\text{C}$  cathode (denoted as  $\text{Co}_9\text{S}_8@\text{C}/\text{NTs}/\text{NVP}$ ) was elaborately assembled according to the working principle illustrated in Figure 6a, with an optimized mass ratio of 1:3.5 for anode to cathode.  $\text{Na}_3\text{V}_2(\text{PO}_4)_3$  was used as a cathode material for full cells because of its effective sodium-ion conductivity and marvelous structural stability.<sup>[2b,8a,25]</sup> The structural characterization and electrochemical performance of commercial  $\text{Na}_3\text{V}_2(\text{PO}_4)_3/\text{C}$  are supplied in Figures S16, S17, Supporting Information. Considering the charge balance principle as well as the irreversible capacity loss during the initial several cycles of the reaction process, the mass ratio of the anode and cathode in full cell was subtly matched in terms of the specific capacities of  $\text{Co}_9\text{S}_8@\text{C}/\text{NTs}$  and NVP in half cell, as presented in Figure 6b. Notably, different mass ratios of the anode and cathode have been explored and the N/P ratio of 1:3.5 manifests the optimal balance between the specific capacity and cycling stability (Figure S18, Supporting Information). The prominent redox peaks overlapping in the charge/discharge stages are portrayed in the cyclic voltammograms

(CVs) (Figure 6c), confirming that the redox reaction possesses extraordinary reversibility. The charge/discharge profiles for the first three cycles of the full cell coincide with each other after the initial cycle, verifying the highly reversible electrochemical process (Figure S19, Supporting Information). The rate performance of the sodium-ion full cell was also recorded in Figure 6d, with specific capacities of 282, 246, 213, 185, and 152  $\text{mAh g}^{-1}$  at 0.1, 0.2, 0.5, 1, and  $2 \text{ A g}^{-1}$  being reached (based on the mass loading of the anode electrode). Furthermore, the galvanostatic charge/discharge (GCD) profiles display similar shapes at different current densities (Figure 6e), emphasizing low polarization. In light of the rate performance, the Ragone plot of the  $\text{Co}_9\text{S}_8@\text{C}/\text{NTs}/\text{NVP}$  (Figure 6f) can be calculated based on the total mass of the cathode and anode, where a remarkable energy density of  $144.32 \text{ Wh kg}^{-1}$  at a power density of  $47.9 \text{ W kg}^{-1}$  can be accomplished, which should be ascribed to the high average operating voltage and creditable rate performance. As reflected in Figure 6g, a high output voltage of 2.33 V with a power density of  $47.9 \text{ W kg}^{-1}$  was available. Figure 6h exhibits an outstanding cycling performance of the full cell at a rate of  $0.1 \text{ A g}^{-1}$ , in which a comparative capacity of

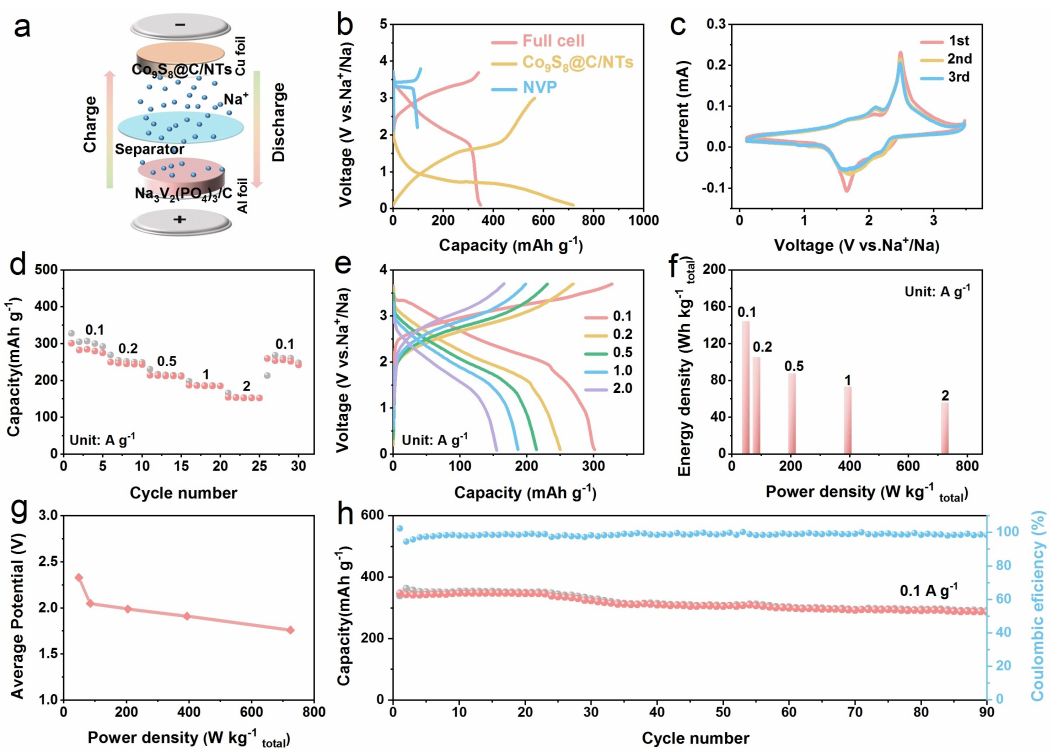


**Figure 6.** Electrochemical performance of the Co<sub>9</sub>S<sub>8</sub>@C/NTs//NVP full cell. (a) Assembly schematic of the full battery; (b) charge/discharge profiles of the half-cell and the Co<sub>9</sub>S<sub>8</sub>@C/NTs//NVP full cell; (c) CV curves at a scan rate of 0.1 mV s<sup>-1</sup>; (d) rate performance at various current densities; (e) charge/discharge profiles at various current densities ranging from 0.1 to 2.0 A g<sup>-1</sup>; (f) Ragone plot of the full cell based on the total mass; (g) The average potential at different power densities; (h) cycling stability of full cell device at 0.1 A g<sup>-1</sup>.

285 mAh g<sup>-1</sup> nearly 100 cycles can still be realized with an admirable capacity retention of 82%, signifying exceptional cycling stability. Additionally, an impressive Coulombic efficiency of about 97% was demonstrated to affirm the reversibility of the cycling period. To conclude, these findings highlight the promising prospect of the practicability of Co<sub>9</sub>S<sub>8</sub>@C/NTs as a reliable competitor for advanced sodium energy storage systems.

### 3. Conclusions

In summary, the composite structure of strongly encapsulating Co<sub>9</sub>S<sub>8</sub> nanoparticles in carbon nanotubes has been obtained by a facile one-pot hydrothermal and subsequent annealing process. Notably, the Co<sub>9</sub>S<sub>8</sub>@C/NTs anode material exhibits enhanced reversible capacity and outstanding cycling stability owing to the synergistic effect in this unique architecture. Furthermore, ex situ characterizations and theoretical calculations reveal that the strong interaction between the Co<sub>9</sub>S<sub>8</sub> nanoparticles and carbon matrix is crucial in enhancing Na<sup>+</sup> absorption ability and accelerating electron transfer dynamics. More encouragingly, the full cell device composed of Co<sub>9</sub>S<sub>8</sub>@C/NTs anode and commercial Na<sub>3</sub>V<sub>2</sub>(PO<sub>4</sub>)<sub>3</sub>/C cathode extends an impressive energy density of 144.32 Wh kg<sup>-1</sup> and a remarkable cyclability of almost 100 cycles with an 82% capacity retention at 0.1 A g<sup>-1</sup>. Our work not only provides an effective approach

to designing metal sulfide/carbon nanocomposites but also highlights their potential application in electrochemical energy storage systems.

### Experimental Section

Experimental details can be found in the Supporting Information.

### Supporting Information

Supporting Information is available from the Wiley Online Library or from the author.

### Acknowledgements

G. Q. Z acknowledges the financial support from the National Natural Science Foundation of China (Grant No. 52072379), the Recruitment Program of Global Experts, and the Fundamental Research Funds for the Central Universities (WK2060000016). The numerical calculations in this paper have been done in the Supercomputing Center of the University of Science and Technology of China at LvLiang Cloud Computing Center of China.

## Conflict of Interests

The authors declare no conflict of interest.

## Data Availability Statement

The data that support the findings of this study are available from the corresponding author upon reasonable request.

**Keywords:** sodium-ion batteries • anode •  $\text{Co}_9\text{S}_8$  • composite structure • strong interaction

- [1] a) W. Zong, C. Yang, L. Mo, Y. Ouyang, H. Guo, L. Ge, Y.-E. Miao, D. Rao, J. Zhang, F. Lai, T. Liu, *Nano Energy* **2020**, *77*, 105189; b) Q. Pan, Z. Tong, Y. Su, S. Qin, Y. Tang, *Adv. Funct. Mater.* **2021**, *31*, 2103912; c) M. Yang, X. Chang, L. Wang, X. Wang, M. Gu, H. Huang, L. Tang, Y. Zhong, H. Xia, *Adv. Mater.* **2023**, *35*, 2208705; d) Y. V. Lim, X. L. Li, H. Y. Yang, *Adv. Funct. Mater.* **2020**, *31*, 2006761; e) D. Ni, W. Sun, Z. Wang, Y. Bai, H. Lei, X. Lai, K. Sun, *Adv. Energy Mater.* **2019**, *9*, 1900036; f) Q. Nannan, S. Yanyan, H. Chao, L. Sainan, L. Zhigao, C. Xinxin, L. Shuquan, F. Guozhao, *J. Energy Chem.* **2022**, *77*, 310.
- [2] a) S. Cheng, K. Yao, K. Zheng, Q. Li, D. Chen, Y. Jiang, W. Liu, Y. Feng, X. Rui, Y. Yu, *Energy Environ.* **2021**, *5*, 592; b) S. Yu, J. Bernt, Z. Shilin, C. Ziru, G. Qinfen, L. Guanjie, Y. Hong, L. Jia-Yang, H. Hai-Yan, Z. Yan-Fang, X. Sailong, L. Huakun, D. Shixue, X. Yao, *Adv. Mater.* **2023**, *35*, 2305149; c) Z. Jian-En, C. Jiahao, P. Yanhua, Z. Yongqian, Z. Akif, L. Xiaoming, *Coord. Chem. Rev.* **2022**, *472*, 214781; d) Y. Huang, X. Hu, J. Li, J. Zhang, D. Cai, B. Sa, H. Zhan, Z. Wen, *Energy Storage Mater.* **2020**, *29*, 121; e) S. Qiao, Q. Zhou, M. Ma, H. K. Liu, S. X. Dou, S. Chong, *ACS Nano* **2023**, 11220.
- [3] a) E. Olsson, J. Yu, H. Zhang, H. M. Cheng, Q. Cai, *Adv. Energy Mater.* **2022**, *12*, 2200662; b) D. Peng, C. Liang, Z. Bao, W. Chunhui, X. Zhiming, Z. Jiafeng, W. Dong, O. Xing, *Renewable Sustainable Energy Rev.* **2021**, *151*, 111640; c) Y. Liu, C. Yang, Q. Zhang, M. Liu, *Energy Storage Mater.* **2019**, *22*, 66; d) D. Wang, L. Cao, D. Luo, R. Gao, H. Li, D. Wang, G. Sun, Z. Zhao, N. Li, Y. Zhang, F. Du, M. Feng, Z. Chen, *Nano Energy* **2021**, *87*, 106185; e) L. Congcong, L. Qiongqiong, V. G. Mikhail, O. Ahmad, G. M. Ignacio, Z. Panpan, H. Martin, P. Antonius Dimas Chandra, H. Huanyu, G. Nikolai, M. Daria, *J. Energy Chem.* **2023**, *79*, 373.
- [4] a) B. Guan, S.-Y. Qi, Y. Li, T. Sun, Y.-G. Liu, T.-F. Yi, *J. Energy Chem.* **2020**, *54*, 680; b) H. Shangguan, W. Huang, C. Engelbrekt, X. Zheng, F. Shen, X. Xiao, L. Ci, P. Si, J. Zhang, *Energy Storage Mater.* **2019**, *18*, 114; c) Y. Feng, M. Xu, T. He, B. Chen, F. Gu, L. Zu, R. Meng, J. Yang, *Adv. Mater.* **2021**, *33*, 2007262; d) Z. Ali, T. Zhang, M. Asif, L. Zhao, Y. Yu, Y. Hou, *Mater. Today* **2020**, *35*, 131; e) Y. Luo, L. Shi, H. He, G. Cong, C. Zhu, J. Xu, *J. Mater. Chem. A* **2021**, *9*, 23537.
- [5] Z. Wenqing, L. Shuya, L. Jiexiang, J. Feng, W. Tianjing, Y. Yue, S. Wei, J. Xiaobo, G. Peng, *Adv. Energy Mater.* **2024**, 2304431.
- [6] a) X. Li, K. Li, S. Zhu, K. Fan, L. Lyu, H. Yao, Y. Li, J. Hu, H. Huang, Y. W. Mai, J. B. Goodenough, *Angew. Chem. Int. Ed.* **2019**, *58*, 6239; b) J. S. Lee, R. Saroha, S. H. Oh, D. H. Shin, S. M. Jeong, J.-K. Kim, J. S. Cho, *Small Methods* **2021**, *5*, 2100195; c) K. Yang, H. Fu, Y. Duan, M. Wang, M. X. Tran, J. K. Lee, W. Yang, G. Liu, *Energy Environ.* **2022**, *6*, 12380; d) X. Hu, Y. Liu, J. Li, G. Wang, J. Chen, G. Zhong, H. Zhan, Z. Wen, *Adv. Funct. Mater.* **2019**, *30*, 1907677; e) L. Huanhuan, C. Yuxin, C. Huiqin, W. Yantao, L. Jinlong, Z. Yanping, Z. Linlin, *J. Energy Chem.* **2023**, *87*, 114; f) C. Deliang, Y. Leyi, W. Ankai, X. Guodong, C. Zhijie, Z. Peipei, C. Yiwang, *Chem. Eng. J.* **2022**, *457*, 141243.
- [7] a) B. Li, Q. Su, L. Yu, J. Zhang, G. Du, D. Wang, D. Han, M. Zhang, S. Ding, B. Xu, *ACS Nano* **2020**, *14*, 17285; b) L. Chen, W. Yang, X. Li, L. Han, M. Wei, *J. Mater. Chem. A* **2019**, *7*, 10331.
- [8] a) Y. Huang, X. Zhu, D. Cai, Z. Cui, Q. Wang, H. Zhan, *J. Energy Chem.* **2020**, *59*, 473; b) W. Zhou, M. Chen, D. Zhao, Q. Wu, J. Dan, C. Zhu, W. Qiu, W. Lei, L.-J. Ma, L. Li, *J. Colloid Interface Sci.* **2022**, *625*, 187; c) D. Guo, Y. Fu, F. Bu, H. Liang, L. Duan, Z. Zhao, C. Wang, A. M. El-Toni, W. Li, D. Zhao, *Small Methods* **2021**, *5*, 2001137.
- [9] a) N. Li, L. Sun, K. Wang, S. Xu, J. Zhang, X. Guo, X. Liu, *J. Energy Chem.* **2020**, *51*, 62; b) C. Hongming, N. Yilin, M. Yanhong, R. Xianzhuo, H. Yingchun, W. Mingshan, L. Woon-Ming, Z. Dan, *J. Alloys Compd.* **2022**, *923*, 166373.
- [10] a) S. Zhang, F. Ling, L. Wang, R. Xu, M. Ma, X. Cheng, R. Bai, Y. Shao, H. Huang, D. Li, Y. Jiang, X. Rui, J. Bai, Y. Yao, Y. Yu, *Adv. Mater.* **2022**, *34*, 2201420; b) Y. Zhao, Q. Fu, D. Wang, Q. Pang, Y. Gao, A. Missiul, R. Nemausat, A. Sarapulova, H. Ehrenberg, Y. Wei, G. Chen, *Energy Storage Mater.* **2018**, *18*, 51; c) Y. Qi, T. Zhang, N. Wu, H. Ding, G. Yu, J. Lian, L. Xu, J. Qiu, S. Li, *ACS Appl. Energ. Mater.* **2021**, *4*, 5574.
- [11] Q. Liu, Z. Hu, Y. Liang, L. Li, C. Zou, H. Jin, S. Wang, H. Lu, Q. Gu, S. L. Chou, Y. Liu, S. X. Dou, *Angew. Chem. Int. Ed.* **2020**, *59*, 5159.
- [12] a) W. Zhong, X. Lv, Q. Chen, M. Ren, W. Liu, G. Li, J. Yu, M. Li, Y. Dai, L. Wang, *ACS Appl. Mater. Interfaces* **2019**, *37850*; b) H. Yang, L. Changlin, P. Shang, Z. Juan, C. Gang, F. Zhongbao, Z. Qiang, A. Abuliti, G. Guoqing, *J. Mater. Sci. Technol.* **2022**, *145*, 210.
- [13] Y. Zhang, R. Zhan, Q. Xu, H. Liu, M. Tao, Y. Luo, S. Bao, C. Li, M. Xu, *Chem. Eng. J.* **2018**, *357*, 220.
- [14] Z. Fen, Z. Yongcai, Z. Geshan, Y. Zhanjun, D. D. Dionysios, Z. Aiping, *Appl. Catal. B* **2018**, *256*, 53.
- [15] a) Y. Lian, F. Chen, H. Kang, C. Wu, M. Zhang, S. Xu, *Appl. Surf. Sci.* **2020**, *507*, 145061; b) X. Li, H. Liang, X. Liu, R. Sun, Z. Qin, H. Fan, Y. Zhang, *Chem. Eng. J.* **2021**, *425*, 130657.
- [16] a) S. Qian, C. Kaiyun, Y. Zhonghai, F. Minxia, D. Zhiyong, W. Jingxiao, C. Kun, T. Fanghua, Z. Yin, Y. Sen, Z. Xuan, *J. Alloys Compd.* **2022**, *902*, 163812; b) M. Yueyue, W. Mengqi, L. Ling, L. Zhanyu, Z. Xiaohui, L. Ruqian, Z. Wenming, *Appl. Surf. Sci.* **2022**, *600*, 154159; c) J. Wang, S. Zhao, J. Wang, X. Xian, *J. Alloys Compd.* **2022**, *919*, 165819.
- [17] a) P. Zhang, M. Cao, Y. Feng, J. Xu, J. Yao, *Carbon* **2021**, *182*, 404; b) Z. Sun, X.-L. Wu, J. Xu, D. Qu, B. Zhao, Z. Gu, W. Li, H. Liang, L. Gao, Y. Fan, K. Zhou, D. Han, S. Gan, Y. Zhang, L. Niu, *Small* **2020**, *16*, 1907670; c) G. Yu, F. Yang, X. Han, Q. Song, J. Zheng, Y. Qi, T. Chen, Q. Shen, J. Qiu, S. Li, *Chin. Chem. Lett.* **2023**, *34*, 108288.
- [18] Y. Wu, R. R. Gaddam, C. Zhang, H. Lu, C. Wang, D. Golberg, X. S. Zhao, *Nano-Micro Lett.* **2020**, *12*, 48.
- [19] a) K. Zhang, Q. He, F. Xiong, J. Zhou, Y. Zhao, L. Mai, L. Zhang, *Nano Energy* **2020**, *77*, 105018; b) X. Li, W. Zhang, J. Cai, H. Yan, M. Cui, G. Wu, M. Li, *Nano Energy* **2019**, *62*, 239.
- [20] a) X. M. Lin, J. H. Chen, J. J. Fan, Y. Ma, P. Radjenovic, Q. C. Xu, L. Huang, S. Passerini, Z. Q. Tian, J. F. Li, *Adv. Energy Mater.* **2019**, *9*, 1902312; b) F. Chen, D. Shi, M. Yang, H. Jiang, Y. Shao, S. Wang, B. Zhang, J. Shen, Y. Wu, X. Hao, *Adv. Funct. Mater.* **2020**, *31*, 2007132.
- [21] a) X. Hu, J. Jia, G. Wang, J. Chen, H. Zhan, Z. Wen, *Adv. Energy Mater.* **2018**, *8*, 1801452; b) M. Yin, D. Zhao, C. Feng, W. Zhou, Q. Jiao, X. Feng, S. Wang, Y. Zhao, H. Li, T. Feng, *ACS Sustainable Chem. Eng.* **2020**, *8*, 6305; c) G. Songwei, H. Yixiang, L. Huaike, Y. Guichu, C. Zhimin, L. Yijie, B. Jie, W. Nü, Z. Qianfan, Y. Yan, Z. Yong, *Energy Storage Mater.* **2023**, *65*, 103170.
- [22] Y. He, C. Dong, S. He, H. Li, X. Sun, Y. Cheng, G. Zhou, L. Xu, *Nano Res.* **2021**, *14*, 4014.
- [23] Y. Zhang, L. Hu, Y. Zhang, X. Wang, H. Wang, *Appl. Catal. B* **2022**, *315*, 121540.
- [24] a) J. Huang, X. Tang, Z. Li, K. Liu, *J. Colloid Interface Sci.* **2018**, *532*, 407; b) L. q. Yu, S. X. Zhao, Q. I. Wu, J. W. Zhao, G. d. Wei, *Adv. Funct. Mater.* **2020**, *30*, 2000427.
- [25] a) C. Wang, D. Du, M. Song, Y. Wang, F. Li, *Adv. Energy Mater.* **2019**, *9*, 1900022; b) Z. Yang, G. Li, J. Sun, L. Xie, Y. Jiang, Y. Huang, S. Chen, *Energy Storage Mater.* **2019**, *25*, 724.

Manuscript received: March 8, 2024

Revised manuscript received: April 11, 2024

Accepted manuscript online: April 21, 2024

Version of record online: May 21, 2024